

Excluding possible sites of high-energy emission in 3C 84

Lena Linhoff¹,¹★ Alexander Sandrock,¹† Matthias Kadler,² Dominik Elsässer¹ and Wolfgang Rhode¹

¹Department of Physics, TU Dortmund University, D-44227 Dortmund, Germany

²Department of Physics, Würzburg University, D-97074 Würzburg, Germany

Accepted 2020 October 26. Received 2020 October 23; in original form 2020 August 14

ABSTRACT

The FR-I galaxy 3C 84, that is identified with the misaligned blazar NGC 1275, is well known as one of the very few radio galaxies emitting gamma-rays in the TeV range. Yet, the gamma-ray emission region cannot be pinpointed and the responsible mechanisms are still unclear. We calculate the optical absorption depth of high-energy photons in the broad-line region of 3C 84 depending on their energy and distance to the central black hole. Based on these calculations, a lower limit on the distance of the emission region from the central black hole can be derived. These lower limits are estimated for two broad-line region geometries (shell and ring) and two states of the source, the low state in 2016 October–December and a flare state in 2017 January. For the shell geometry, we can place the emission region outside the $\text{Ly}\alpha$ radius. For the ring geometry and the low flux activity, the minimal distance between the black hole, and the gamma-ray emission region is close to the $\text{Ly}\alpha$ radius. In the case of the flaring state (ring geometry), the results are not conclusive. Our results exclude the region near the central black hole as the origin of the gamma-rays detected by *Fermi*–LAT and Major Atmospheric Gamma-Ray Imaging Cherenkov. With these findings, we can constrain the theoretical models of acceleration mechanisms and compare the possible emission region to the source’s morphology resolved by radio images from the Very Long Baseline Array.

Key words: acceleration of particles – astroparticle physics – galaxies: individual: NGC 1275 – galaxies: jets – gamma-rays: galaxies – radio continuum: galaxies.

1 INTRODUCTION

The elliptical radio galaxy 3C 84 ($z = 0.0176$) is located in the Perseus cluster and is one of the closest and brightest radio galaxies. Because of its proximity, it has been observed and studied quite well over the years with different ground- and space-based detectors and telescopes. The Large Area Telescope (LAT) onboard the *Fermi* satellite discovered high-energy gamma-ray emission from the active galactic nucleus (AGN) counterpart NGC 1275 in 2008 (Abdo et al. 2009). In the very high-energy (VHE) regime, the same source was detected by the Major Atmospheric Gamma-Ray Imaging Cherenkov Telescopes (MAGIC) in 2014 (Aleksić et al. 2014). Additionally, very long baseline interferometry (VLBI) experiments such as the Very Long Baseline Array (VLBA; Lister et al. 2018) detected the source at a variety of wavelengths and were able to resolve the source’s morphology. NGC 1275 is therefore one of the very rare AGN detected at TeV energies whose jets are not directly pointed towards the Earth. Further objects classified as TeV-radio galaxies are Centaurus A, M 87, IC 310, 3C 264, and PKS 0625-35 (Rani 2019).

The VLBI data reveal separated radio emission regions in the centre of the source and two jets at a greater distance from the core. Due to Doppler dimming, the northern counterjet appears much fainter. VLBA observations from the Boston University Blazar

Monitoring Program (VLBA-BU-BLAZAR; Jorstad & Marscher 2016) and the RadioAstron (Kardashev et al. 2013) reveal the limb-brightened structure of a newly restarted jet close to the radio core of the source (Nagai et al. 2014), which is assumed to be the location of the central black hole. The fact that we measure both gamma and radio emission and can resolve the source’s morphology, offers the unique opportunity to locate the gamma-ray emission region and study the jet’s physics, its acceleration mechanisms and the angle to the line of sight. Regarding this angle to the line of sight, former publications are ambiguous. VLBI experiments calculated the viewing angle to be 30° – 55° in Walker, Romney & Benson (1994) and 65° in Fujita & Nagai (2016). *Fermi*–LAT reported an angle of 25° in Abdo et al. (2009). The latest attempt was accomplished by the MAGIC collaboration, where the viewing angle was estimated to be $<17^\circ$ (Ansoldi et al. 2018), which is an apparent contradiction to the previous measurements. Some models assume the gamma-emission region close to the central black hole, e.g. the Magnetospheric Gap Model (Aharonian, Barkov & Khangulyan 2017). Other models (e.g. the Spine-Layer model by Ghisellini, Tavecchio & Chiaberge (2005) or the jets-in-jet model by Giannios, Uzdensky & Begelman 2009) support the idea that the gamma-rays are produced further away from the central black hole somewhere along the jet. The idea of the innermost region as the origin of gamma-ray emission contradicts the assumption of photoabsorption in the broad-line region (BLR). However, the acceleration of photons to TeV energies outside the BLR challenges the models locating the gamma-rays’ origin exclusively close to the central black hole.

★ E-mail: lena.linhoff@tu-dortmund.de

† Now at National Research Nuclear University MEPhI, Moscow

Previous publications already found evidence for a gamma-ray emission region outside the BLR for other AGNs. For example, Meyer, Scargle & Blandford (2019) analysed the gamma-ray variability of a set of six flat-spectrum radio quasars and Costamante et al. (2018) studied 106 blazars detected by *Fermi*-LAT.

This paper is structured as follows: First, we describe the used data in Section 2. In Section 3, the calculations regarding the optical depth are explained and applied in a fit to the combined spectral energy distribution (SED) in Section 4. Results are presented and discussed in Sections 6 and 7, respectively.

2 DATA

For this study, we use data obtained by the MAGIC telescopes and the *Fermi*-LAT in the energy range from MeV to TeV. The SEDs and light curves in the TeV range were published by the MAGIC collaboration, see Aleksić et al. (2014) and Ansoldi et al. (2018). For the light curve and SEDs in the MeV–GeV range, we perform the data analysis with measurements provided by the *Fermi*-LAT collaboration (see Section 7). See subsection 2.2 and Section 7 for further details. To set or results in context with the morphology of the source, we use radio images provided by the VLBA-BU-BLAZAR Program (Jorstad & Marscher 2016).

2.1 MAGIC

The MAGIC telescopes are a system of two Cherenkov telescopes of 17 m mirror diameter located on the Canary Island of La Palma, Spain, at 2200 m height (Aleksić et al. 2016a). The detector has a field of view of 3.5° and is capable of measuring the energies of gamma-ray particles from 50 GeV to 50 TeV. To detect gamma-ray events of a weak source in the VHE regime with imaging air Cherenkov telescopes, nights without moonlight and good weather conditions are needed. Furthermore, the source has to be visible from the facility’s site and its flux must exceed the sensitivity threshold. A weak source like NGC 1275 ($F = 1.19 \pm 0.03 \times 10^{-10} \text{ cm}^{-2} \text{ s}^{-1}$) is therefore not always detectable and the resulting light curve is not as densely sampled compared to light curves from the space-bound telescope *Fermi*-LAT or radio telescopes (cf. Fig. 1). MAGIC has observed NGC 1275 since 2010 at irregular distributed times. For this work, we use the SEDs published in Ansoldi et al. (2018) and light curves published in Aleksić et al. (2014) and Ansoldi et al. (2018). The data set Ansoldi et al. (2018) collected contains 63 h of data taken between 2016 September and 2017 February at zenith distances from 12° to 50° . Because of bad weather conditions, 7 h were omitted. The standard data analysis performed on this data set is described in Aleksić et al. (2016b). Within this period, MAGIC detected a significant gamma-ray flare, where for 2 d the flux was 50 times higher than the mean flux measured until then (Fig. 1). We use SEDs measured during the low state phase (2016/09–2016/12) and the flare (2017/01/01). The term ‘low state’ refers here to a phase, where the source was quite active compared to the decades before, but, in contrast to the ‘flaring state’, of lower flux and less variability.

2.2 *Fermi*-LAT

The LAT is a gamma-ray detector on the *Fermi* Gamma-Ray Space Telescope covering the energy range from 20 MeV to 300 GeV (Atwood et al. 2009). In comparison to ground-based gamma-ray detectors, the duty cycle and the field of view is extremely large covering 20 percent of the sky at any time. Therefore, the light curve is sampled densely over years (since 2008) without large gaps.

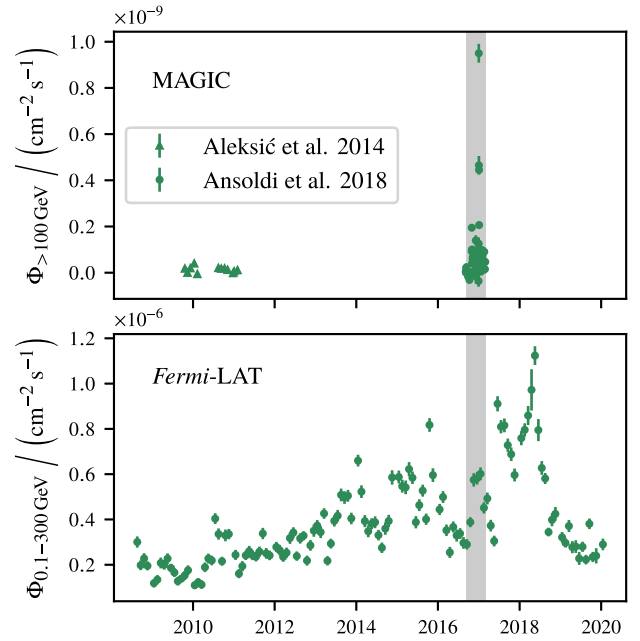


Figure 1. Light curves of NGC 1275 measured by MAGIC and *Fermi*-LAT between 2008 and 2020. *Upper panel:* gamma-ray flux above 100 GeV obtained by MAGIC in 2009–2011 and in 2017, (Aleksić et al. 2014; Ansoldi et al. 2018). *Lower panel:* *Fermi*-LAT observations from 2008 August 4 to 2020 February 16 in an energy range of 0.1–300 GeV with monthly binning. The grey-shaded area marks the data used for the modelling the SED in Section 4.

For the light curve shown in Fig. 1, we analyse data from 2008 August 4 to 2020 February 16. The SEDs in Fig. 4 are produced using data simultaneously taken with MAGIC, from 2016 September to 2016 December and at the flare night on 2017 January, the first. We produce the light curve and spectrum using FERMITOOLS (version 1.0.5) and FERMPY (version 0.17.4, Wood et al. 2017) with the instrument response function P8R3_SOURCE_V2 and the galactic interstellar emission model gll_iem_v07. In all cases, we use publicly available data provided at eventclass P8R3_SOURCE (128). All sources from the *Fermi*-LAT 8 yr point source list (FL8Y) in a region of 20° around the source position are included within our model. The energy range is selected from 100 MeV to 300 GeV.

2.3 VLBA

The VLBA is a radio interferometer consisting of 10 25 m antennas spread over the USA with a maximum distance of 8600 km between Hawaii and the Virgin Islands (Napier et al. 1994). The VLBA has operated since 1994 at multiple wavelengths and is capable of measuring radio sources with brightness temperature $> 10^5$ K. 3C 84 is one of the best-monitored sources and is part of the VLBA-BU-BLAZAR program, which provides measurements at 43 GHz (Jorstad & Marscher 2016). For this work, we use the total intensity maps and the CLEAN model files provided by the VLBA-BU-BLAZAR program, cf. Fig. 2. The clean images used here are also publicly available (see Section 7) and we did not perform additional calibration or image cleaning. The radio images are used here to discuss the constraints on the gamma-ray emission region in the context of the source morphology resolved in the radio images. Details of the source morphology are discussed in Section 6.1.

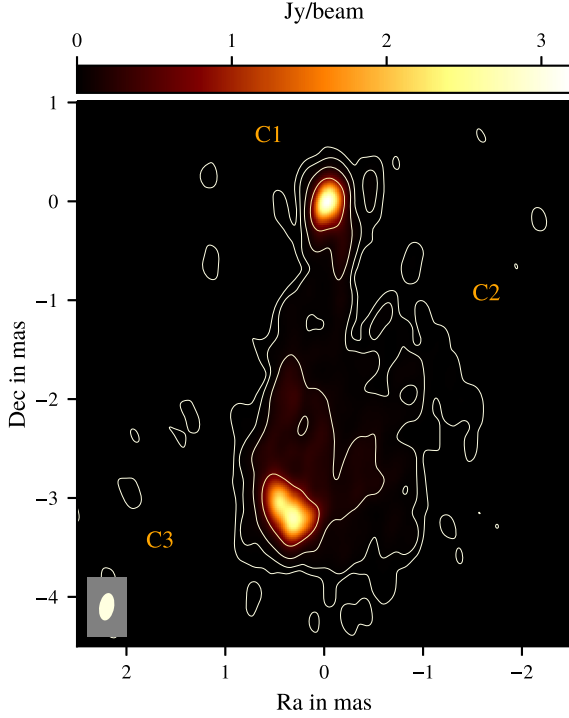


Figure 2. VLBA 43 GHz image from the Boston University Blazar Monitoring Program of 3C 84 on 2016-07-04 (contours at 0.004, 0.02, 0.12, 0.61, 3.19 Jy beam⁻¹). Beam size: 0.28×0.15 mas with a beam position angle of -10° .

3 OPTICAL ABSORPTION

A relatively new approach locating the gamma-ray emission region can be taken by examining the optical depth $\tau_{\gamma\gamma}$ of the BLR. In Finke (2016), the production of gamma-radiation via external Compton scattering of seed photons from the accretion disc, the BLR, and the dust torus were investigated. These seed photons, which can be scattered to very high energies, are in turn responsible for gamma-absorption due to pair production. For this work, we concentrate on the photon fields within the BLR, where gas cools efficiently by Ly α line emission of neutral hydrogen. Due to pair production of gamma-rays with energy $E_\gamma = m_e c^2 \epsilon_1$ in a photon field with energy density distribution $u(\epsilon, \Omega; \ell)$, the gamma-ray spectrum is attenuated by a factor $e^{-\tau_{\gamma\gamma}}$. $\tau_{\gamma\gamma}$ is given by (e.g. Dermer et al. 2009)

$$\tau_{\gamma\gamma}(\epsilon_1) = \int_{R_{\text{jet}}}^{\infty} d\ell \int_0^{2\pi} d\phi \int_{-1}^1 d\mu (1 - \cos \psi) \times \int_0^{\infty} d\epsilon \frac{u(\epsilon, \Omega; \ell)}{\epsilon m_e c^2} \sigma_{\gamma\gamma} \left[\frac{\epsilon \epsilon_1 (1+z)}{2} (1 - \cos \psi) \right]. \quad (1)$$

Here, ℓ denotes the position along the jet and ψ is the angle between the photons; by assuming that the gamma-rays travel in the direction of the jet we have $\cos \psi = \mu$ and the integration over ϕ becomes trivial for the axially symmetric photon fields we consider in this work. Depending on the spatial distribution of the emitting material in the BLR, different specific formulae are obtained for ring and shell geometries. Photons with energies lower than 20 GeV (in the source frame) can escape the BLR unabsorbed. For further details, see Finke (2016).

The distance of the gamma-ray emission region to the central black hole R_{jet} is given in times of the Ly α radius. The Ly α radius refers to the region within the BLR, where Ly α emission is produced. This emission line is the brightest in the BLR spectrum and has the greatest

energy density, which is by a factor of 160 higher than the H β energy density. Therefore, it is the most important line causing Compton scattering and $\gamma\gamma$ absorption. There are indications of stratification of the BLR, i.e. that different lines are predominantly emitted at different radii (Poutanen & Stern 2010). We use the compilation of lines, velocities and radii of Finke (2016; table 5), based on Vanden Berk et al. (2001), Kollatschny (2003), and Peterson & Wandel (1999).

Due to the proximity of 3C 84 (redshift $z = 0.0176$), we take no absorption by extragalactic background light into account, based on calculations by Dominguez et al. (2011).

In a distance up to 10 times the Ly α radius, the escaping gamma radiation depends on the structure of the BLR. Taking the shape of the BLR into account, two geometries are discussed in previous works: a flattened ring geometry and a spherical shell geometry. Since the geometry has a strong impact on the BLR's opacity for gamma-rays, we use both geometries for comparison. The shell is the most common geometry for modeling the BLR, which is used in a variety of publications (e.g. Ghisellini & Madau 1996; Donea & Protheroe 2003; Celotti, Ghisellini & Fabian 2007; Dermer et al. 2009; Abolmasov & Poutanen 2017). It assumes the gas clouds to be distributed in a geometrically thick shell around the black hole. Depending on further assumptions, this spherical shell is pierced by a jet cone with varying opening angle or can be divided into two hemispheres by the accretion disc. Since the shell model has some limitations (see Lei & Wang 2014 for further reading), an alternative geometry of a flat ring was introduced (e.g. Tavecchio & Ghisellini 2012; Grier et al. 2017). In this case, gas clouds are arranged in a ring, which can be interpreted as a cross-section of the shell at a certain angle to the jet direction. Following Finke (2016), we assume the radius of the ring to be perpendicular to the jet axis. The $\tau_{\gamma\gamma}$ obtained using the flattened ring geometry is in general lower and pair production starts at higher energies. Therefore, R_{jet} is expected to be smaller for the same particle energies. Both geometries are theoretical approaches. The true shape of 3C 84's BLR remains unknown and we cannot state which geometry is more likely.

Following Finke (2016), Fig. 3 show the optical depth $\tau_{\gamma\gamma}$ for 3C 84 as a function of the photon energy E and the distance of the emission region from the central black hole R_{jet} , with redshift $z = 0.0176$, $L(\text{H}\beta) = 8.94 \times 10^{40} \text{ erg s}$ (Punsly et al. 2018) and $R(\text{H}\beta) = 2.37 \times 10^{16} \text{ cm}$. $R(\text{H}\beta)$ is given in Finke (2016, Appendix) by

$$R(\text{H}\beta) = 10^{16.94 \pm 0.03} \left(\frac{L(5100\text{\AA})}{1 \times 10^{44} \text{ erg s}} \right)^{0.533 \pm 0.035} \text{ cm} \quad (2)$$

with the relation (Greene & Ho 2005)

$$\left(\frac{L(5100\text{\AA})}{1 \times 10^{44} \text{ erg s}} \right) = \left(\frac{L(\text{H}\beta)}{1.425 \pm 0.007 \times 10^{42} \text{ erg s}} \right)^{0.8826 \pm 0.0039}. \quad (3)$$

4 SED FIT

To model the SED with an absorbed spectrum, we combined the measurements of *Fermi*-LAT and MAGIC to cover a greater energy range. To evaluate the optical depth at different states of flux activity, we use one data set measured during the low state phase and another during the TeV flare at the beginning of 2017 January (Ansoldi et al. 2018). The resulting SED is fitted with a log-parabola function, multiplied with an optical absorption term

$$\frac{dN}{dE} = N_0 \left(\frac{E}{E_0} \right)^{-(\alpha + \beta \log(\frac{E}{E_0}))} \cdot e^{-\tau(E, R_{\text{jet}})}. \quad (4)$$

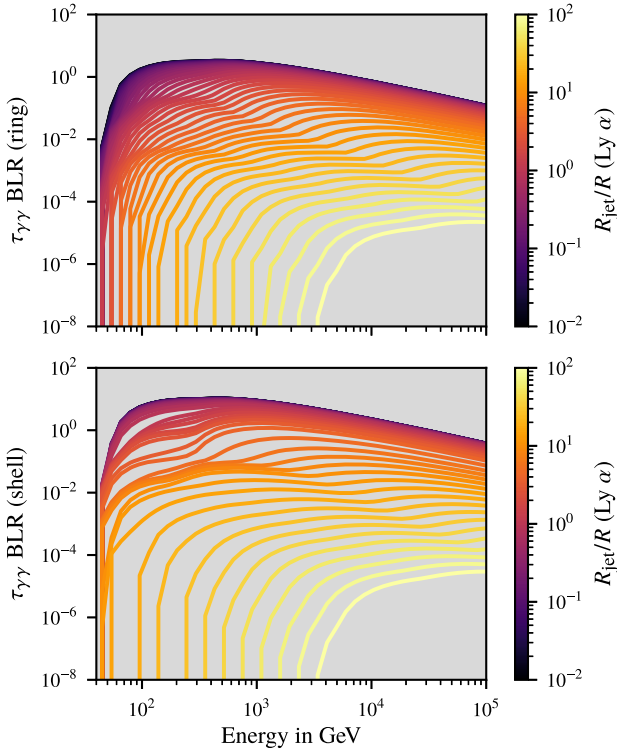


Figure 3. Optical depth in the broad-line region depending on particle energy (observers frame) and position of the emission region R_{jet} along the jet using the flattened ring geometry (above) spherical shell geometry (below).

With this function, we can fit the value of R_{jet} and obtain in this way an estimation for the distance of the gamma-ray emission region from the central black hole. If we assume that all gamma-ray emission comes from a single emission region, absorption only takes place in the BLR and the log-parabola assumption for the shape of the unabsorbed spectrum holds true, R_{jet} pinpoints the position of the emission region, within the fitted parameter's uncertainties. If other photon fields are present (e.g. dust torus, accretion disc, CMB, etc.), high-energy photons experience additional absorption that contributes to the optical depth. In this case, R_{jet} is a lower limit for the distance of the gamma-ray emission region from the central black hole, since the emission can originate further downstream in the jet, but not closer to the central black hole.

As described before, we model the SED for both geometries, the spherical shell geometry, and the flattened ring geometry, see Fig. 4. The data used here only include statistical errors. The resulting fit parameters can be found in Table 1. To be sure that the fit results for R_{jet} are not sensitive to fluctuations based on the systematic uncertainties of the data points, we add these for the absolute energy scale and redo the fit. *Fermi*-LAT reported this uncertainty to be -5 per cent and 2 per cent (Ackermann et al. 2012), for MAGIC, we use ± 15 per cent as found by Aleksić et al. (2016c). Fit results under consideration of the systematic uncertainties of the absolute energy scale can be found in Appendix A, Table A1. Including the systematic uncertainties, the estimation for R_{jet} is shifted mostly to higher values and varies in most cases around 10 per cent. This does not affect the conclusions we draw from our calculations.

For all states and geometries the most likely R_{jet} is $>R(\text{Ly}\alpha)$, such that the emission region is at the edge or outside the BLR of $\text{Ly}\alpha$ emission. In the case of the fit for the flare state and ring geometry, the fit value for R_{jet} is not reliable due to the big uncertainty.

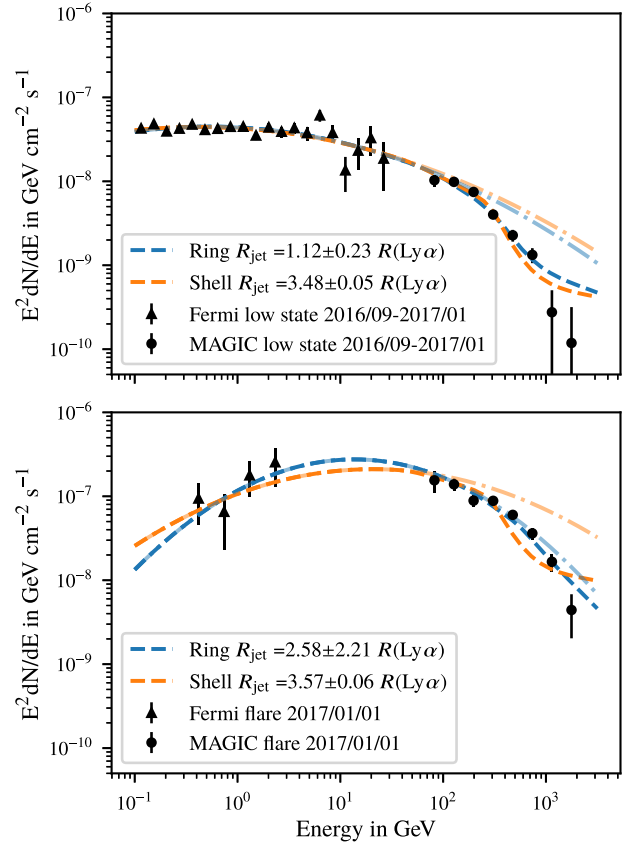


Figure 4. Combined spectral energy distribution (*Fermi*-LAT and MAGIC) for the low state 2016/09–2016/12 (above) and the flaring state on 2017/01/01 (below). The dashed lines indicate the best-fitting results using an absorbed log-parabola spectrum for the two geometries. For comparison, the unabsorbed log-parabola spectrum is shown (dot-dashed lines) with $\tau(E, R_{\text{jet}})$ set to 0 (cf. equation 4). The blueish dot-dashed line refers to the ring geometry, the orange line to the shell geometry. Note that R_{jet} is given in terms of the 5 $\text{Ly}\alpha$ radius.

Table 1. Fit parameter for log-parabola function with absorption during the low state 2016/09 to 2016/12 (upper table) and the flaring state on 2017/01/01 (lower table).

Parameter	Ring (low)	Shell (low)
N_0 in $10^{-8}\text{GeV}^{-1}\text{cm}^{-2}\text{s}^{-1}$	4.39 ± 0.18	4.30 ± 0.17
E_0 in GeV	1	1
α	2.06 ± 0.03	2.07 ± 0.02
β	0.05 ± 0.01	0.04 ± 0.01
R_{jet} in $R(\text{Ly}\alpha)$	1.12 ± 0.23	3.48 ± 0.05
R_{jet} in mas, $\theta = 17^\circ$	0.002	0.007
R_{jet} in mas, $\theta = 65^\circ$	0.007	0.022
Parameter	Ring (flare)	Shell (flare)
N_0 in $10^{-8}\text{GeV}^{-1}\text{cm}^{-2}\text{s}^{-1}$	11.69 ± 4.09	10.67 ± 6.63
E_0 in GeV	1	1
α	1.35 ± 0.20	1.55 ± 0.33
β	0.13 ± 0.03	0.07 ± 0.05
R_{jet} in $R(\text{Ly}\alpha)$	2.58 ± 2.21	3.57 ± 0.06
R_{jet} in mas, $\theta = 17^\circ$	0.005	0.007
R_{jet} in mas, $\theta = 65^\circ$	0.016	0.022

In both states, the fit using the ring geometry performs slightly better than using the shell geometry, see χ^2 values in Appendix A, Table A2. For comparison, we calculate the angular distances corresponding to R_{jet} in mas, see Table 1, assuming two different viewing angles, published by Ansoldi et al. (2018; 17°) and Fujita & Nagai (2016; 65°). For all calculations, we use the relation of $R(\text{Ly}\alpha) = 0.27 R(\text{H}\beta) = 6.39 \times 10^{15} \text{ cm}$ (table 5, Finke 2016) and the distance of the source as $d = 62.5 \text{ Mpc}$ (Tully et al. 2013).

5 RESULTS

We calculate the distance of the gamma-ray emission region from the black hole for two BLR geometries and two flux states of the source. For the most common and well-described shell geometry, we obtain values for $R_{\text{jet}} > 1$ and can therefore clearly state the gamma-ray emission region to be outside the BLR. As expected, (see Section 3) R_{jet} is smaller for the ring geometry in both states of flux activity. For the ring geometry, less BLR material covers or surrounds the jet's cross-section and absorbs gamma-ray emission, which we assume to originate along the jet. As a consequence, the gamma-ray emission region can be placed closer to the black hole. In the case of the low flux activity state, R_{jet} is close to the $\text{Ly}\alpha$ radius, hence the emission region is not near the black hole. For the flaring state, the fit result comes with great uncertainty and is therefore not conclusive.

As stated in Section 4, the calculated values have to be understood as a minimal distance of the emission region from the black hole in case other photon fields are present and contribute to the photoabsorption. Taking this into account, the sub-parsec scale jet is also a possible emission region.

Since we converted R_{jet} into mas (cf. Table 1), we are able to relate those distances with the resolution capacity of radio images. Note that R_{jet} is of the order of μas and thus not resolved by radio images of 3C 84, even with beam sizes of $\approx 0.05 \times 0.05 \text{ mas}^2$, which were achieved by RadioAstron (Giovannini et al. 2018) and the Global Millimeter VLBI Array (Kim et al. 2019a). The radio component C1, which is close to or even hosting the black hole, is therefore a possible gamma-ray emission region. Since its inner structure cannot be resolved further by the beam of currently operating telescopes, it is probably smaller, and we cannot identify which part of the source's core is producing radio emission and which part is a proper location for gamma-ray production.

Comparing the flaring state and the low state of the source, we find that the minimal distance of R_{jet} grows from the low state to the flaring state. This could be a hint that other emission mechanisms at locations further away from the core are responsible for the short flare in the VHE regime detected by MAGIC.

6 DISCUSSION

6.1 Results in the context of the source's radio morphology

3C 84 consists of a bright and compact core region (called C1), which launches a limb-brightened jet in south direction (Nagai et al. 2010) and is considered to host the black hole. This core component C1 has an average size of $0.12 \pm 0.01 \text{ mas}$ in the 43-GHz-VLBA images, whereas the clean beam size is $0.28 \times 0.15 \text{ mas}^2$. Even comparing the scales of R_{jet} to the currently best-resolved images from RadioAstron (beam size $0.05 \times 0.05 \text{ mas}^2$), a radius of $1\text{--}10 \mu\text{as}$ is inside C1. C1 can thus not be excluded as emission region at least as long as the component cannot be resolved further by VLBI experiments.

A remarkable feature in 3C 84's recent past was the jet component called C3 that was ejected from the core in 2003. C3 has been moving

along the jet in south direction and had its brightness maximum in 2016 (cf. Fig. 2, left) before it broadened and decreased in surface brightness (cf. Fig. 2, right). Furthermore, there has been a very faint region located south-east to C1 (called C2), which dissociated from the core in the 1990s and is barely detectable in the 43-GHz observations. Plasmoid ejections from the central region of a galaxy are often considered as an origin of the gamma-ray emission, but in the case of C3, neither MAGIC nor *Fermi*-LAT was operating at the ejection time so that no gamma-ray data are available for this event. Since there has been no new component ejected during the gamma-ray flare MAGIC detected in 2017, there have to be other mechanisms producing high-energetic photons. None the less, our calculations do not exclude the variable hotspot C3 as a possible gamma-ray emission region.

Our results are in agreement with the results of former publications. Nagai et al. (2016) assumed the short gamma-ray flares originating from the limb-brightened structure of the sub-parsec scale jet. In the same publication, the long-term rising trend in gamma-ray emission, *Fermi*-LAT reported (cf. Fig. 1), is assumed to be originating from C3. The fact that *Fermi*-LAT measured a rapid decrease in the MeV gamma-ray flux after C3 expanded and lost its radio luminosity is in accordance with this hypothesis. Hodgson et al. (2018) found correlations between gamma and radio light curves in C1 before 2015 and in C3 after 2015, which also indicates that both C1 and C3 contribute to the gamma-ray emission from 3C 84.

6.2 Size of the emitting region

Based on the flux variability during the gamma-ray flare, Ansoldi et al. (2018) calculated the size of the gamma-ray emitting region as $R = \delta \cdot 1.1 \times 10^{15} \text{ cm}$, which is equal to $R = \delta \cdot 1 \times 10^{-3} \text{ mas}$, where δ is the Doppler factor. As well as for the viewing angle, the estimations for δ are ambiguous. Hovatta et al. (2009) found a Doppler factor of 0.3, Kim et al. (2019b) calculated $\delta \approx 1.1$ and Aleksić et al. (2014) reported a Doppler factor of 2 - 4. Even for larger Doppler factors, an emission region of this size can be located within the radio components C1, since our results exclude just a small part of C1. Taking the uncertain location of the black hole into account, the innermost core of C1 can also be considered as a possible emission region, if the black hole is not located at the centre of C1.

6.3 Acceleration mechanisms

Various models exist to explain high-energy photons coming from AGNs. Some of them place the gamma-ray emission region close to the black hole and can be considered very unlikely based on our results. For example, the Magnetospheric Model (Aharonian et al. 2017) predicts ultrahigh energy gamma-ray emission due to gaps in the magnetosphere of an AGN's central black hole. These gaps occur at low accretion rates, when not enough charged particles are induced to provide a full screening of the electric field, which is caused by the rotation of the compact black hole. A particle accelerated to very high energies by the electric field can leave the magnetosphere. In this scenario, the gamma-ray emission has its origin in the innermost core of the source, which is excluded as an emission region by this work. Furthermore, the magnetospheric model was also considered to be unlikely in Ansoldi et al. (2018) because the flux measured by MAGIC exceeds the upper limit of flux predicted with this model by a factor of ≈ 3 .

Other models, namely the Spine-Layer Model (Tavecchio & Ghisellini 2014) or the magnetic reconnection model (Giannios et al.

2009), which locate the responsible mechanisms further downstream the jet, are not in direct conflict with our results. But former publications reveal incompatibilities between model and measured data for both models. The spine-layer model is not capable of explaining the energies at TeV range measured by MAGIC during the flare in 2017 January. In the concept of the magnetic reconnection model, extremely strong magnetic fields are required to produce TeV photons, which only exist in the surrounding of the central black hole. See Ansoldi et al. (2018) for further reading.

7 CONCLUSIONS

In this paper, we combine data and analysis results of the radio-loud AGN 3C 84 (NGC 1275) obtained by *Fermi*–LAT, MAGIC, and the VLBA. We analyse the *Fermi*–LAT data and combine our resulting SEDs with SEDs at higher energies published by the MAGIC collaboration (Ansoldi et al. 2018). A fit with a model of an absorbed log–parabola spectrum is applied to the combined SEDs. The absorption term depends on the geometry of the BLR, which is why two models for a shell and a ring geometry are used. The fit results are discussed in the context of the radio morphology, which we review based upon the radio maps provided by the BU-BLAZAR Monitoring program.

Since MAGIC detected a flare in 2017 January, we analyse the data of two states; the low state, containing data from 2016 September until 2016 December and the flaring state, containing the data of the flare on 2017 January, first. For both states, we constrain the possible gamma-ray emission region by calculating the optical depth for high-energy photons along the jet.

Given the assumptions Finke (2016) made in his work, we find that gamma-ray emission is only possible for distances close to or greater than the $\text{Ly } \alpha$ radius and probably further outside the BLR. We can therefore exclude the surrounding area of the black hole as the origin of the gamma-ray emission based on our calculations. In case of the low-state SED fit, R_{jet} comes close to the $\text{Ly } \alpha$ radius, if taking the uncertainty into account. But even a distance of $\approx 0.9 R(\text{Ly } \alpha)$ still excludes regions very close to the black hole. Only in case of fitting the ring geometry model to the flaring state SED, the results are not conclusive due to the great uncertainty.

The radio component C1 is not completely excluded by these restrictions. Depending on the location of the central black hole, which is still unclear, C1 could lie partly or completely outside the BLR.

Our results are in line with previous findings regarding the distance of the gamma-ray emission region from the black hole. Meyer et al. (2019) calculated distances in the same order of magnitude for different sources with similar approaches as used in this publication.

These results challenge all models, which assume the emission region for high-energy photons close to the central black hole. Nevertheless, our result is in accordance with other models, placing the emission region of gamma-rays further away from the core. But other achievements in the last years, regarding the viewing angle, the luminosity, or the Doppler factor of the source, pose a challenge to all these models in one way or another. At present, no model is able to explain the gamma-ray emission from 3C 84 concerning the variety of multiwavelength measurements and analysis results from all operating instruments. The location of the black hole and the emission mechanisms are still subjects of ongoing research. Furthermore, our results elucidate the geometry's impact on the assumptions regarding the gamma-ray emission region, which also has to be investigated further. Especially in the VHE regime, continuous observations in the low state are missing, mostly because of the limited sensitivity

for a weak source such as NGC 1275. Until now, one orphan flare proves VHE gamma-ray activity from this source.

In the near future, the upcoming Cherenkov Telescope Array (Acharya et al. 2017) will technically be able to detect and monitor NGC 1275 even in a low state. It comes with a lower sensitivity threshold compared to all present observing Cherenkov telescopes and is currently under construction on La Palma and in Chile. From that new era of telescopes, we expect more insights into the activity of TeV-radio galaxies and their acceleration mechanisms.

ACKNOWLEDGEMENTS

This study has used 43-GHz-VLBA data from the VLBA-BU Blazar Monitoring Program (VLBA-BU-BLAZAR; <http://www.bu.edu/blazars/VLBAproject.html>), funded by NASA through the Fermi Guest Investigator Program. The VLBA is an instrument of the National Radio Astronomy Observatory. The National Radio Astronomy Observatory is a facility of the National Science Foundation operated by Associated Universities, Inc. Part of this work is supported by Deutsche Forschungsgemeinschaft (DFG) -project number 124020371- within the Collaborative Research Center SFB 876 "Providing Information by Resource-Constrained Analysis", DFG project number 124020371, SFB project C3. We thank Jeffery Hodgson for fruitful discussions and helpful comments.

DATA AVAILABILITY

The data used in this paper are publicly available to access and download as follows:

- (i) MAGIC data from 2016/17 as used in Ansoldi et al. (2018): http://vobs.magic.pic.es/fits/mfits/base/MAGIC_2018_NGC_1275.fits.
- (ii) MAGIC data from 2010/11 as used in Aleksić et al. (2014): http://vobs.magic.pic.es/fits/mfits/base/MAGIC_2014_NGC_1275.fits.
- (iii) *Fermi*–LAT data can be downloaded at <https://fermi.gsfc.nasa.gov/cgi-bin/ssc/LAT/LATDataQuery.cgi>.
- (iv) VLBA data can be downloaded at https://www.bu.edu/blazars/VLBA_GLAST/0316.html.

REFERENCES

- Abdo A. A. et al., 2009, *ApJ*, 699, 31
- Abolmasov P., Poutanen J., 2017, *MNRAS*, 464, 152
- Acharya B. et al., 2017, , Science with the Cherenkov Telescope Array. World Scientific Press, Singapore
- Ackermann M. et al., 2012, *Astropart. Phys.*, 35, 346
- Aharonian F., Barkov M., Khangulyan D., 2017, *ApJ*, 841, 61
- Aleksić J. et al., 2014, *A&A*, 564, A5
- Aleksić J. et al., 2016a, *Astropart. Phys.*, 72, 61
- Aleksić J. et al., 2016b, *Astropart. Phys.*, 72, 76
- Aleksić J. et al., 2016c, *Astropart. Phys.*, 72, 76
- Ansoldi S. et al., 2018, *A&A*, 617, A91
- Atwood W. et al., 2009, *ApJ*, 697, 1071
- Celotti A., Ghisellini G., Fabian A. C., 2007, *MNRAS*, 375, 417
- Costamante L., Cutini S., Tosti G., Antolini E., Tramacere A., 2018, *MNRAS*, 477, 4749
- Dermer C. D., Finke J. D., Krug H., Böttcher M., 2009, *ApJ*, 692, 32
- Dominguez A. et al., 2011, *MNRAS*, 410, 2556
- Donea A.-C., Protheroe R., 2003, *Astropart. Phys.*, 18, 377
- Finke J. D., 2016, *ApJ*, 830, 94
- Fujita Y., Nagai H., 2016, *MNRAS*, 465, L94
- Ghisellini G., Madau P., 1996, *MNRAS*, 280, 67
- Ghisellini G., Tavecchio F., Chiaberge M., 2005, *A&A*, 432, 401

Giannios D., Uzdensky D. A., Begelman M. C., 2009, *MNRAS*, 395, L29
 Giovannini G. et al., 2018, *Nat. Astron.*, 2, 472
 Greene J. E., Ho L. C., 2005, *ApJ*, 630, 122
 Grier C., Pancoast A., Barth A., Fausnaugh M., Brewer B., Treu T., Peterson B., 2017, *ApJ*, 849, 146
 Hodgson J. A. et al., 2018, *MNRAS*, 475, 368
 Hovatta T., Valtaoja E., Tornikoski M., Lähteenmäki A., 2009, *A&A*, 494, 527
 Jorstad S., Marscher A., 2016, *Galaxies*, 4, 47
 Kardashev N. et al., 2013, *Astron. Rep.*, 57, 153
 Kim J.-Y. et al., 2019a, *A&A*, 622, A196
 Kim J.-Y. et al., 2019b, *A&A*, 622, A196
 Kollatschny W., 2003, *A&A*, 407, 461
 Lei M., Wang J., 2014, *PASJ*, 66, 1
 Lister M., Aller M., Aller H., Hodge M., Homan D., Kovalev Y., Pushkarev A., Savolainen T., 2018, *ApJS*, 234, 12
 Meyer M., Scargle J. D., Blandford R. D., 2019, *ApJ*, 877, 39
 Nagai H. et al., 2010, *PASJ*, 62, L11
 Nagai H. et al., 2014, *ApJ*, 785, 53
 Nagai H., Chida H., Kino M., Orienti M., D’Ammando F., Giovannini G., Hiura K., 2016, *Astron. Nachr.*, 337, 69
 Napier P. J., Bagri D. S., Clark B. G., Rogers A. E., Romney J. D., Thompson A. R., Walker R. C., 1994, *Proc. IEEE*, 82, 658
 Peterson B. M., Wandel A., 1999, *ApJ*, 521, L95
 Poutanen J., Stern B., 2010, *ApJ*, 717, L118
 Punsly B., Marziani P., Bennert V. N., Nagai H., Gurwell M. A., 2018, *ApJ*, 869, 143
 Rani B., 2019, *Galaxies*, 7, 23
 Tavecchio F., Ghisellini G., 2012, preprint (arXiv:1209.2291)
 Tavecchio F., Ghisellini G., 2014, *MNRAS*, 443, 1224
 Tully R. B. et al., 2013, *AJ*, 146, 86
 Vanden Berk D. E. et al., 2001, *AJ*, 122, 549
 Walker R., Romney J., Benson J., 1994, *ApJ*, 430, L45

Wood M., Caputo R., Charles E., Di Mauro M., Magill J., Perkins J., 2017, *Proceedings of Science, ICRC2017*, 824

APPENDIX A: TABLES

Table A1. Fit parameter R_{jet} in $R(\text{Ly}\alpha)$ for log-parabola function with absorption taking the systematic uncertainty of the absolute energy scale of *Fermi*–LAT and MAGIC into account. (Ackermann et al. 2012; Aleksić et al. 2016c).

State	Geometry	$R_{\text{jet}, +\Delta E}$	$R_{\text{jet}, -\Delta E}$
Low	Ring	1.23 ± 0.33	1.13 ± 0.23
Low	Shell	3.69 ± 0.30	3.64 ± 0.01
Flare	Ring	3.47 ± 4.41	2.24 ± 1.64
Flare	Shell	4.74 ± 0.01	3.89 ± 0.07

Table A2. χ^2 values for SED fit in Section 4, Table 1.

State	Geometry	DOF	χ^2
Low	Ring	23	45.57
Low	Shell	23	40.52
Flare	Ring	7	12.54
Flare	Shell	7	37.56

This paper has been typeset from a \LaTeX file prepared by the author.